Triangular Magnet Emergent from Noncentrosymmetric Sr$_{0.94}$Mn$_{0.86}$Te$_{1.14}$O$_6$ Single Crystals

Kalimuthu Moovendaran, Raju Kalaivanan, I. Panneer Muthuselvam, K. Ramesh Babu, Suheon Lee, C. H. Lee, Khasim Saheb Bayikadi, Namasivayam Dhenadhayalan, Wei-Tin Chen, Chin-Wei Wang, Yen-Chung Lai, Yoshiyuki iizuka, Kwang-Yong Choi, Vladimir B. Nalbandyan, and Raman Sankar*

Cite This: https://doi.org/10.1021/acs.inorgchem.2c01585

Read Online

ACCESS | Metrics & More | Article Recommendations | Supporting Information

ABSTRACT: We report the successful growth of high-quality single crystals of Sr$_{0.94}$Mn$_{0.86}$Te$_{1.14}$O$_6$ (SMTO) using a self-flux method. The structural, electronic, and magnetic properties of SMTO are investigated by neutron powder diffraction (NPD), single-crystal X-ray diffraction (SCXRD), thermodynamic, and nuclear magnetic resonance techniques in conjunction with density functional theory calculations. NPD unambiguously determined octahedral (trigonal antiprismatic) coordination for all cations with the chiral space group $P312$ (no. 149), which is further confirmed by SCXRD data. The Mn and Te elements occupy distinct Wyckoff sites, and minor anti-site defects were observed in both sites. X-ray photoelectron spectroscopy reveals the existence of mixed valence states of Mn in SMTO. The magnetic susceptibility and specific heat data evidence a weak antiferromagnetic order at $T_N = 6.6$ K. The estimated Curie–Weiss temperature $\theta_{CW} = -21$ K indicates antiferromagnetic interaction between Mn ions. Furthermore, both the magnetic entropy and the ^{125}Te nuclear spin–lattice relaxation rate showcase that short-range spin correlations persist well above the Néel temperature. Our work demonstrates that Sr$_{0.94(2)}$Mn$_{0.86(3)}$Te$_{1.14(3)}$O$_6$ single crystals realize a noncentrosymmetric triangular antiferromagnet.
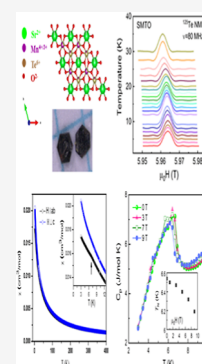
1. INTRODUCTION

Over decades, noncentrosymmetric magnetic oxide materials have garnered enormous research interest as they epitomize fascinating physical properties such as multiferroicity and magnetoelectricity.[1–7] In this context, layered A^{2+}M^{4+}TeO$_6$ and A^{3+}M^{3+}TeO$_6$ tellurates are of interest. This family comprises three trigonal structure types based on honeycomb-type MTeO$_6$ layers of edge-shared octahedra. Two of them are superstructures of the rosiaite (PbSb$_2$O$_6$) structure-type (centrosymmetric space group $P\bar{3}1m$)[8] with all cations in octahedral coordination but differ in the M/Te ordering pattern. In AMTeO$_6$ (A = rare earth or Bi; M = Cr,[9–11] Mn,[11,12] or Fe[11,13,14]), M and Te alternate along the principal axis. This results in doubling the cell edge c but the structure retains the inversion center, space group being $P\bar{3}1c$ (or $P2_1/c$ for BiMnTeO$_6$[11,12] distorted by the Jahn–Teller effect). On the other hand, in AGeTeO$_6$ (A = Sr,[15] Mn, Cd, or Pb[16]), PbMnTeO$_6$,[17] and BiMTeO$_6$ (M = Al and Ga),[18] M/Te only order within the honeycomb layer without changing cell volume, thus eliminating mirror plane and inversion center (chiral space group $P312$). BaGeTeO$_6$ belongs to the same space group but has doubled a cell edge c because of the different oxygen stacking (ABBA vs ABAB) and prismatic (rather than antiprismatic) coordination of Ba^{2+}.[15] Due to identical octahedral radii of Mn^{4+} and Ge^{4+}, the same structure type may be expected for BaMnTeO$_6$.

In the majority of the phases discussed above, partial M/Te disorder (antisite defects) was found during structure refine-ments. However, it seems highly probable that this is only an apparent effect due to stacking faults, whereas each individual layer may be completely ordered. For AMnTeO$_6$ (A = Sr[19] or Pb[20]) having similar unit cell sizes to their Ge counterparts, entirely different non-centrosymmetric structures (space group $P\bar{6}2m$) were initially reported with all three cation types in a trigonal-prismatic oxygen environment. This was extremely strange for Mn^{4+} and Te^{6+} and was never found for these small cations among hundreds of studied structures.[21] Later, this structure for PbMnTeO$_6$ was corrected to be $P312$,[17] and we expected the same for SrMnTeO$_6$.

Singularly, the M/Te ordering patterns have strong ramifications on sublattice magnetism. For the perfect M/Te ordering, we expect that a triangular lattice is derived from half-filled honeycomb layers. As such, the degree of the M/Te ordering determines the presence or absence of geometrical frustration. This has relevance to spin liquid physics. For triangular and Kagome systems with higher spin numbers $S > 1$, classical spin liquids have been sought after. Till date, an exotic short-range order or a weak magnetic order has been reported in NiGa$_2$S$_4$ ($S = 1$),[22] SrCr$_{9p}$Ga$_{12-9p}$O$_{19}$ ($S = 3/2$),[23]

A
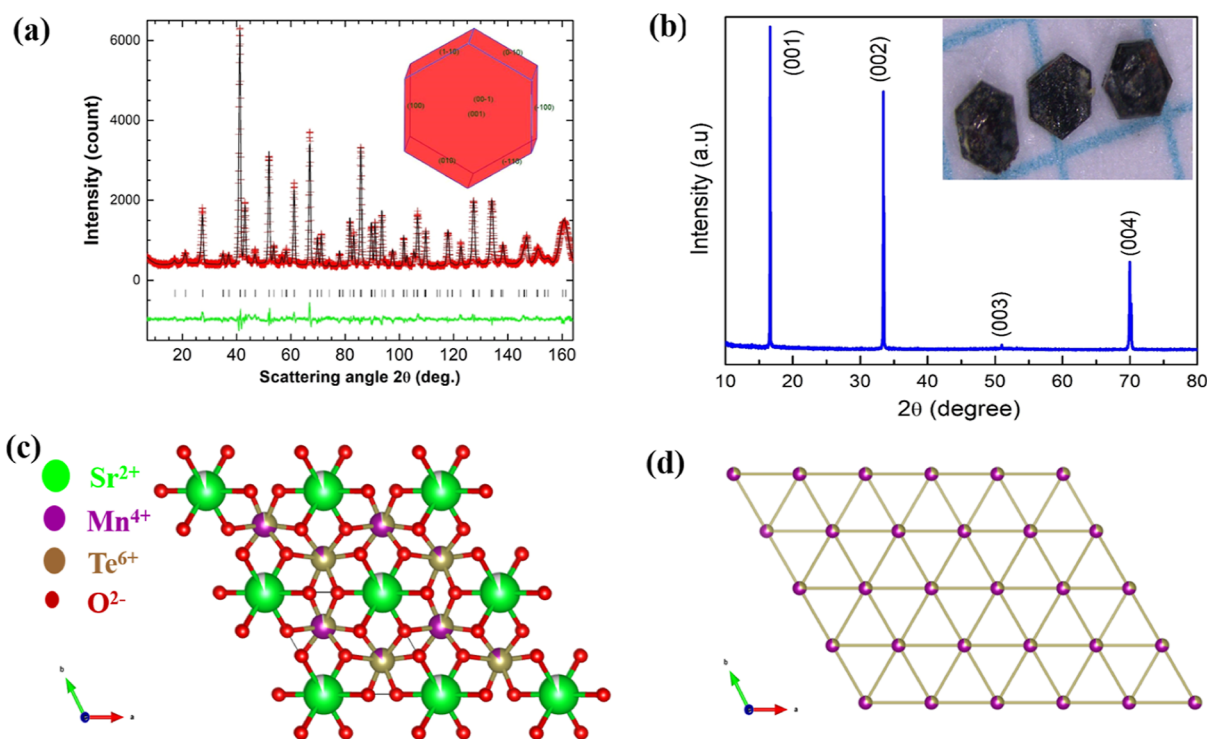
Figure 1. (a) Rietveld refinement fit with trigonal symmetry with $P312$ space group of crushed SMTO single crystals using NPD at RT. The observed, calculated, and difference patterns are shown in red crosses and black and green lines, respectively. (b) X-ray diffraction pattern taken from the largest face of a SMTO single crystal in the Bragg−Brentano geometry. (c) Crystal structure of SMTO with minor anti-site defects was observed in both sites of Mn and Te. (d) Triangular lattice of Mn ions emerging from Mn and Te ordering. The insets of Figure 1a,b represent the morphology and optical image of the as-grown crystal.

and Fe-jarosite $KFe_3(OH)_6(SO_4)_2$.[24] On the other hand, the disordered $J_1−J_2$ honeycomb antiferromagnets may be realized. In the classical limit $(S \rightarrow \infty)$, the system is Néel ordered for $J_2/J_1 < 1/6$ and spirally ordered for $J_2/J_1 > 1/6$.[25]

In this study, we present the successful growth of $Sr_{0.94(2)}Mn_{0.86(3)}Te_{1.14(3)}O_6$ (SMTO) single crystals and detailed structural, magnetic, thermal, and nuclear magnetic resonance (NMR) characterizations in combination with theoretical calculations. Our experimental and theoretical studies confirm the chiral space group $P312$. The title compound undergoes weak antiferromagnetic ordering at T_N = 6.6 K. The magnetic specific heat and ^{125}Te NMR data evidence the persistence of short-ranged spin correlations up to $3T_N$, highlighting reduced dimensionality thanks to the cation ordering.

2. EXPERIMENTAL DETAILS

A polycrystalline sample of SMTO was prepared by the solid−state reaction method using $Sr(OH)_2$, $MnCO_3$, and TeO_2 of purity 99.95% (Alfa Aesar). The mixture of reagents was calcined at 600 °C in an open atmosphere for 24 h, then ground and further sintered at 750 °C for 48 h. The schematic diagram of the flux growth method is sketched in Figure S1. An imbalance between the flux and pristine powder compounds leads to the formation of secondary Mn_3O_4, Sr_2MnTeO_6, and so forth phases. To resolve this issue, we have examined various fluxes (NaCl + KCl, TeO_2, $SrCl_2$, etc.) and succeeded in obtaining the SMTO single phase using a mixture of two different fluxes [$Sr(OH)_2$ and TeO_2]. The polycrystalline powder of SMTO was mixed with $Sr(OH)_2$ and TeO_2 with a ratio of 1:2:2 that were thoroughly ground and placed in a platinum (Pt) crucible. The Pt crucible was placed in a muffle box furnace and heated at the rate of 5 °C/min to 1200 °C soaked for 10 h; furthermore, it was slowly cooled to 900 °C for 200 h and finally proceeded to 30 °C. The

grown single crystals are leached out from the flux by using deionized water and NaOH.

The single-crystal plane was identified by making use of the Cu $K\alpha$ radiation with Bragg−Brentano geometry with a Bruker D2 Phaser diffractometer. A further experiment in neutron powder diffraction (NPD) was conducted at the ECHIDNA diffractometer,[26] Australian Nuclear Science and Technology Organisation, Australia. The pulverized SMTO sample of around 1 g was loaded into a vanadium can, and the pattern was obtained at room temperature (RT) with a wavelength of 1.622 Å. The collected patterns were analyzed with the Rietveld method using the FullProf Suite software.[27] Single-crystal X-ray diffraction (SCXRD) data of SMTO were collected with an Xcalibur Atlas Gemini diffractometer, with Mo $K\alpha$ (λ = 0.71073 Å) radiation with a graphite monochromator. A 0.080 × 0.050 × 0.050 mm³ crystal was mounted, and the data collection was carried out at 100 K with a theta range up to 49.972°. CrysAlis Pro software was used for indexing, cell refinement, and data reduction, and ShelXL[28] was used for structure refinement. The crystal structure of SMTO was further investigated by high-resolution transmission electron probe micro-analyzer (HR-TEM) (Jeol-7400) at 200 kV. TEM micrographs were analyzed by using GATAN microscope software.

The magnetic susceptibility measurements were carried out using a superconducting quantum interference device vibrating sample magnetometer (SQUID VSM) (Quantum Design, USA). The specific heat data were measured using a standard relaxation method with a physical property measurement system (Quantum Design, USA). ^{125}Te (gyromagnetic ratio γ_N = 13.4523 MHz/T) NMR experiments were conducted using a home-made NMR spectrometer (MagRes) and an Oxford Teslatron PT superconducting magnet in the temperature range of 4−30 K. To record ^{125}Te NMR spectra, we adopted a standard Hahn-echo (spin-echo) sequence with a $\pi/2$ pulse length of 3−5 μs. In the process of tracking all peaks, we varied a resonance frequency at a fixed magnetic field $\mu_0 H \sim 6$ T. To determine the spin−lattice relaxation rate $1/T_1$, we used the standard saturation recovery method with 100 saturation pulse train. The

nuclear magnetization M versus elapse time t was fitted to a single exponential recovery function $[M_{\infty} - M(t)] \sim A \exp(-t/T_1)$, where A is the fitting parameter. The chemical compositions of grown single crystals were examined using a field emission electron microprobe (JEOL FE-EPMA JXA-8500F) equipped with wavelength X-ray-dispersive spectrometers. The X-ray photoelectron spectroscopy (XPS) measurement was examined using a VG Scientific ESCALAB 250 spectrometer, to identify the oxidation state and chemical composition.

3. RESULTS AND DISCUSSION

3.1. Crystal Structure: NPD and SCXRD. The atomic structure, diffraction patterns, and crystal habit are presented in Figure 1. The pulverized SMTO sample was examined by the NPD technique. Benefited from the distinct neutron scattering lengths of manganese and tellurium (−3.73 and 5.80 fm, respectively) and high (compared to XRD) scattering power of oxygen, equal to that of Te, the crystal structure and element distribution of SMTO can be determined precisely. Previously, $SrMnTeO_6$ was reported to adopt a crystal structure with space group $P\bar{6}2m$,[19] where Te and Mn occupied the same prismatic Wyckoff site as distributed randomly. In contrast, our NPD results at RT revealed that the obtained sample has the empirical formula $Sr_{0.94}Mn_{0.86}Te_{1.14}O_6$ and crystalizes in trigonal symmetry with $P312$ space group (no. 149). The Mn and Te elements occupy distinct octahedral Wyckoff sites, and minor anti-site defects were observed in both sites. The high-resolution NPD pattern and the Rietveld refinement results are shown in Figure 1a and Table 1. The obtained lattice parameters are in good agreement with those reported in the literature.[19] The new structural study disproves the previous structure with prismatic coordination of all cations.

In addition, the SCXRD data of SMTO single crystal at 100 K showed the empirical formula $Sr_{0.94}Mn_{0.81}Te_{1.17}O_6$ with

$P312$ space group. The crystal data, structure solution, refinement parameters, atomic coordinates, and displacement parameters are listed in Tables S1−S3. Furthermore, chemical composition analysis was carried out using the EPMA method (see the Supporting Information for details). It resulted in the gross formula: $SrMn_{0.757(9)}Te_{1.128(3)}O_x$. It is concluded that the quantitative analysis of the empirical formula from the EPMA of the SMTO is in fairly good agreement with the NPD and the SCXRD result, with slight deficiency at the Sr site. Based on both structural data sets, the most accurate composition of SMTO is $Sr_{0.94(2)}Mn_{0.86(3)}Te_{1.14(3)}O_6$. To provide charge balance, there should be $0.16Mn^{3+}$ and $0.70Mn^{4+}$, resulting in 3.81 as average oxidation number of Mn. It should be noted that the resultant "partially ordered" structure is consistent with previously reported $PbMnTeO_6$.[17]
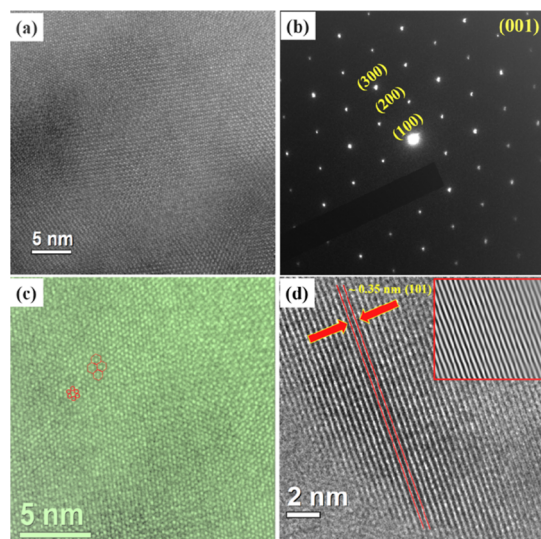
The diffraction pattern of the flat single crystals shows $(00l)$ reflections (Figure 1b), indicating that the geometric hexagonal shape is preferably along the ab-plane. The morphology and optical image of the SMTO crystal are shown in the insets of Figure 1a,b, respectively. The SMTO crystal structure is shown in Figure 1c, with all cations in octahedral coordination and partial Mn/Te inversion. However, we suppose that this may be a fictitious effect caused by the faulty stacking of perfectly ordered individual layers. Ideally, SMTO constitutes a triangular lattice of Mn ions, as shown in Figure 1d. The bond distances agree well with the corresponding sums of ionic radii (Table 2). Bond valences could not be calculated accurately due to mixed occupancies.

Table 2. Selected Interatomic Distances in SMTO, Space Group $P312$, Compared with Sums of Ionic Radii

atom connections	bond lengths, [Å]		sum of radii,[29] [Å]
	NPD	SCXRD	
Sr−O	2.5215(9) × 6	2.519(2) × 6	2.54
$(Te_{0.90}Mn_{0.10})_1$−O	1.929(1) × 6	1.936(3) × 6	1.92
$(Mn_{0.76}Te_{0.24})_2$−O	1.911(1) × 6	1.918(3) × 6	1.93

3.2. High-Resolution TEM. Figure 2 presents HR-TEM analysis performed on SMTO crystal powder. Figure 2a exhibits the high-resolution honeycomb lattice of the crystal system, and Figure 2b shows the selective area electron diffraction (SAED) analysis performed in the (001) direction. The obtained diffraction pattern represents the planes of (100), (200), (300), and so forth. The d-spacing calculations from TEM analysis for the crystal planes perfectly match with the reported material,[19] as shown in the XRD pattern. Figure 2c reveals the high-resolution hexagonal lattice of the SMTO crystal system. The hexagonal lattice is indicated in red color lines. Figure 2d shows high-resolution lattice analysis performed for the (101) plane with d-spacing ∼ 0.35 nm; the inset presents the fast Fourier transformations (FFT) performed to confirm the crystal plane more accurately. Our TEM analysis further confirms the SMTO crystal structure and its honeycomb lattice more precisely.

3.3. X-ray Photoelectron Spectroscopy. XPS measurement was performed to identify the oxidation state and chemical composition of SMTO crystals. The XPS spectrum of each Sr, Mn, Te, and O element was recorded and then deconvoluted into individual peaks, as shown in Figure S2. The XPS spectrum of Sr shows a characteristic broad peak of Sr 3d in the energy range of 126−138 eV. The peak was

Table 1. Refinement Results of the SMTO: NPD and SCXRD Data

measurement[a]		NPD[b]	SCXRD[c]
temperature/K		300	100
wavelength/Å		1.622	0.71073
a/Å		5.09119(3)	5.1083(4)
c/Å		5.38449(6)	5.3782(6)
V/Å³		120.869(2)	121.54(2)
Sr	Occ	0.938(7)	0.946(4)
	U_{eq}/Å² × 10³	11.3(1)	4(1)
Te1	Occ	0.899(4)	0.877(1)
Mn1	Occ	0.101(4)	0.115(5)
	U_{eq}/Å² × 10³	11.3(1)	5(1)
Mn2	Occ	0.760(4)	0.694(4)
Te2	Occ	0.240(4)	0.292(7)
	U_{eq}/Å² × 10³	11.3(1)	4(1)
O	X	0.3784(2)	0.3768(6)
	Y	0.3811(2)	0.3795(4)
	z	0.6994(2)	0.6994(4)
	U_{eq}/Å² × 10³	11.3(1)	6(1)

[a]For the crystal refinement, both NPD and SCXRD data adopt trigonal space group $P312$ (no. 149), where the atomic positions are Sr $1a$ (0, 0, 0), Te1/Mn1 $1f$ (2/3, 1/3, 1/2), Mn2/Te2 $1c$ (1/3, 2/3, 1/2), and O $6l$ (x, y, z). [b]Reliability factors of NPD Rietveld refinement are R_p = 4.25, R_{exp} = 4.39, R_{wp} = 5.40, and χ^2 = 1.51. U_{eq} values were constrained to be equal. [c]For more details, see Tables S1−S3.

Figure 2. HR-TEM analysis of the SMTO crystal system: (a) high-resolution frustrated honeycomb lattice of SMTO, (b) SAED analysis in the (001) direction, (c) magnified honeycomb lattice indicated with red hexagons, and (d) lattice analysis of the (101) plane SMTO (inset: FFT analysis).

deconvoluted into two distinct peaks at ~130.8 and 133.3 eV corresponding to Sr $3d_{5/2}$ and $3d_{3/2}$, respectively, representing the existence of the Sr^{2+} oxidation state (Figure S2a). The XPS spectrum of Mn displays characteristic peaks of Mn 2P in the binding energy of 635−660 eV (Figure S2b). The peaks located at a lower (~643.5 eV) and higher (~654.5 eV) binding energy are characteristic of Mn $2P_{3/2}$ and Mn $2P_{1/2}$, respectively, which are further deconvoluted into four peaks. The two peaks observed at 643.1 and 654.1 eV correspond to the Mn^{3+} oxidation state, whereas the presence of Mn^{4+} results in peaks at 645.4 and 655.8 eV. This result validates the presence of manganese in both the +3 and +4 oxidation states.

Similar to Mn, two characteristic peaks of Te were observed in the binding energy of 570−595 eV (Figure S2c). The peaks located at a lower (~576.8 eV) and higher (~587.4 eV) binding energy are ascribed to Te^{6+} with the splitting of Te $3d_{5/2}$ and Te $3d_{3/2}$, respectively. The characteristic peak of O 1s was observed at ~530 eV, which is deconvoluted into two peaks at ~529.7 and 532.5 eV (Figure S2d). A broad peak at 529.7 eV is attributed to metal oxide in the crystal lattice, whereas the peak at 533.5 eV corresponds to the defect oxide sites.

3.4. Magnetic Susceptibilities and Magnetization.
Figure 3a represents the temperature-dependent dc magnetic susceptibility $\chi(T)$ of SMTO single crystal measured in an applied magnetic field of $\mu_0H = 0.1$ T along the c-axis and the ab plane. Its inverse $1/\chi(T)$ is plotted in Figure 3b. We observed no discernible splitting of $\chi(T)$ for both $H\|c$ and $H\|ab$ between the zero-field-cooled (FC) and FC paradigms, excluding the possibility of spin-glass or inhomogeneous magnetism. Figure 3b shows fittings of $1/\chi(T)$ to the Curie−Weiss (CW) law $\chi(T) = C/(T - \theta_{CW})$, where C is the Curie constant and θ_{CW} is the CW temperature. The extracted CW parameters are $C = 1.59$ cm^3 K mol^{-1} and $\theta_{CW} = -21$ K, indicative of the presence of dominant antiferromagnetic interactions between Mn ions. The estimated effective magnetic moment $\mu_{eff} = 3.85$ μ_B per formula unit confirms the mixed-valence state of manganese and accords well with the theoretical spin-only values expected for a weighted average of Mn^{3+} ($S = 2$, 4.89 μ_B per Mn^{3+}) and Mn^{4+} ($S = 3/2$, 3.83 μ_B per Mn^{4+}) for the two variants of the gross formula. Given that 0.16 Mn^{3+} ions and 0.70 Mn^{4+} ions are present in the formula unit, the effective paramagnetic moment per formula unit is given as $\mu_{eff} = \{4[0.16 \times 2(2 + 1) + 0.70 \times (3/2(3/2 + 1))]\}^{1/2}$ μ_B/f.u = 3.79 μ_B/f.u. Thus, the obtained experimental $\mu_{eff} = 3.85$ μ_B is fairly close to the theoretically estimated value, taking into account composition uncertainties in $Sr_{0.94(2)}Mn_{0.86(3)}Te_{1.14(3)}O_6$.
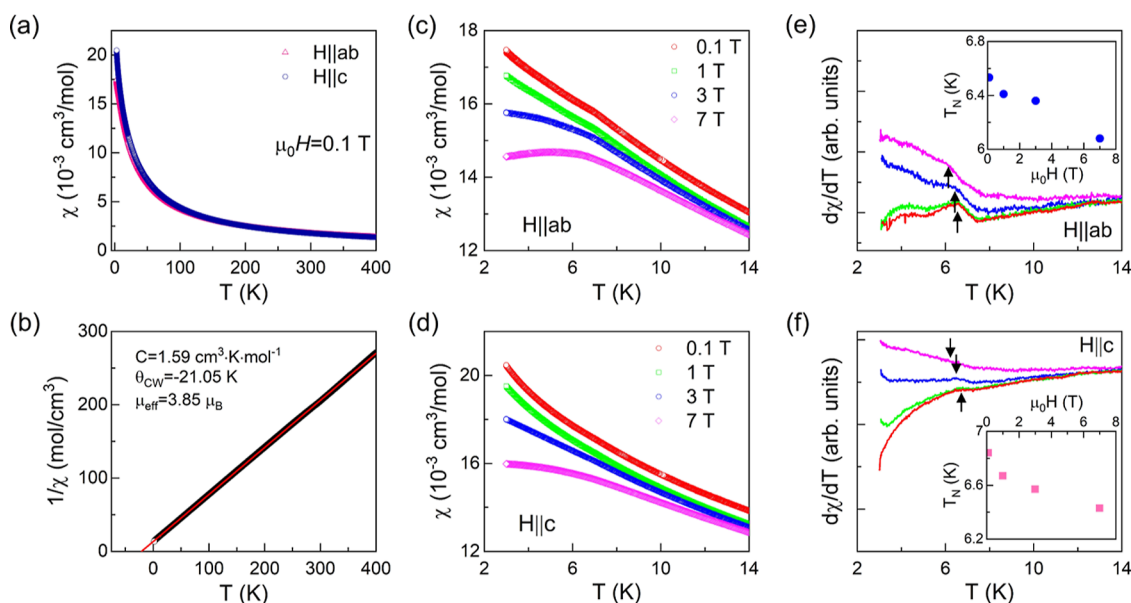
Figure 3. (a) Temperature dependence of magnetic susceptibility $\chi(T)$ for an applied magnetic field $\mu_0H = 0.1$ T, (b) inverse magnetic susceptibility of a pulverized single crystal powder; the solid red line represents a fit of $1/\chi(T)$ to the CW law. The magnified $\chi(T)$ behavior at various external magnetic fields of 0.1−7 T; (c) for $H\|ab$ and (d) for $H\|c$. The first derivative of $\chi(T)$ for (e) $H\|ab$ and (f) $H\|c$ in different magnetic fields. The insets show the field dependence of T_N.

A gradual increase in $\chi(T)$ with decreased temperature (~3 K) was observed in both directions. A small bending at $T_N \sim$ 6.88 K is apparent for only $H\|ab$, while becoming obscured for $H\|c$, as shown in Figure 3c,d. The bending anomaly indicates a weak magnetic ordering, further confirmed by specific heat data (see below). In addition, with increasing magnetic field from 0.1 to 7 T, $\chi(T)$ develops a broad maximum for $H\|ab$. On the other hand, the anomaly is less apparent for the $H\|c$ data. The first derivative of $\chi(T)$ enables us to determine precisely weak magnetic transitions, as shown in Figure 3e,f. The field-dependent magnetic transition temperature for $H\|ab$ and $H\|c$ is plotted in the inset of Figure 3e,f. In both directions, the magnetic transition is shifted toward the lower temperature side with increasing field.

We comment that the frustration parameter $f = |\theta_{CW}|/T_N \sim$ 3.05[30] suggests the presence of some degree of spin frustration in the SMTO compound.[31] Noticeably, $f = 3.05$ of SMTO is somewhat larger than $f \sim 2.16$ of PbMnTeO$_6$, lending support to the notion that the (B, B′) cation ordering somewhat amplifies magnetic frustration by forming a geometrically frustrated triangular lattice and that SMTO contains a small amount of the antisite defects.

Figure 4 shows the isothermal magnetization $M(H)$ as a function of an applied magnetic field measured at $T = 3$ K for
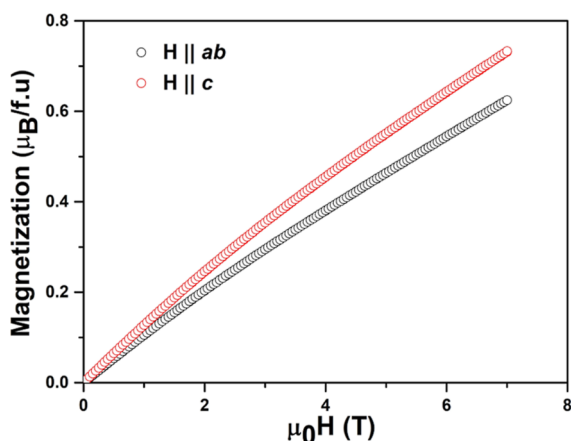

Figure 4. Magnetization curve of SMTO measured at $T = 3$ K.

$H\|ab$ and $H\|c$. For both directions, we found that there is no noticeable anomaly in the magnetic fields up to 7 T. $M(H)$ shows a quasilinear increase while exhibiting a slight bending at about 2.6 T for $H\|c$ and 1.3 T for $H\|ab$. The measured field window is not wide enough to reach the saturation magnetic moment of $M_S = gS\mu_B \approx 2.93\mu_B$ and to identify a linear increase typical for antiferromagnets.

3.5. Heat Capacity. Figure 5a shows the specific heat (C_p) as a function of temperature for single-crystal SMTO. To single out a magnetic contribution, the isostructural non-magnetic compound PbGeTeO$_6$ was used, yet SMTO and PbGeTeO$_6$ showed a marked difference in the high-temperature C_p (not shown here). In an alternative way, we calculate the lattice contribution to the heat capacity C_{lat} with the Debye model

$$C_p(T) = 9rN_A k_B \sum_{i=1,2} C_i \left(\frac{T}{\theta_D^i}\right)^3 \int_0^{x_D^i} \frac{x^4 e^x}{(e^x - 1)^2} dx \quad (1)$$
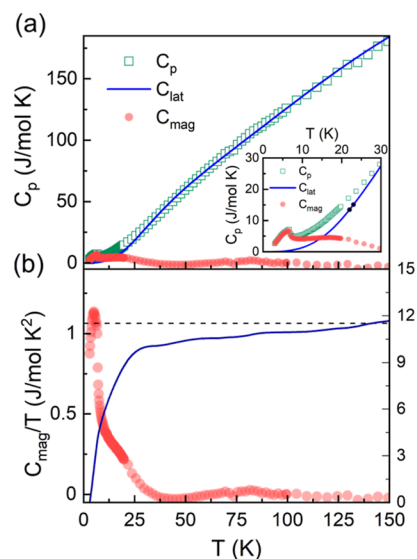

Figure 5. (a) Temperature dependence of the heat capacity (C_p) for SMTO single crystal together with the calculated lattice contribution (C_{lat}) to the heat capacity using the two Debye models described in eq 1 of the main text. The pink circles represent the magnetic specific heat $C_{mag} = C_p - C_{lat}$. The inset shows the enlarged C_p at low temperatures. (b) Magnetic heat capacity divided by temperature (pink circles) and the magnetic entropy (blue solid lines) as a function of temperature. The horizontal dashed line denotes the theoretical value of 10.21 J/(mol·K) for a mixed $S = 3/2$ and $S = 2$ system.

where r is the number of atoms per formula unit, N_A is the Avogadro number, k_B is the Boltzmann constant, and θ_D is the Debye temperature. As evident in Figure 5a, the calculated lattice contributions with the two Debye temperatures of $\theta_D^1 = 691(8)$ K and $\theta_D^2 = 177(3)$ K well reproduced the experimental data above 50 K. The extracted magnetic contribution $C_{mag}(T) = C_p(T) - C_{lat}(T)$ exhibits a small maximum at $T_N = 6.54$ K and a broad hump around 15 K (see the inset of Figure 5a). The former corroborates that the bending anomaly in the $\chi(T)$ data corresponds to long-range magnetic ordering. On the other hand, the latter gives another energy scale related to a two-dimensional triangular lattice.

From $C_{mag} = C_p(T) - C_{lat}$, we evaluate the magnetic entropy (S_{mag}) by integrating C_{mag}/T over T. The C_{mag}/T and S_{mag} are plotted together in Figure 5b. 85.5% of the total magnetic entropy is released below the Weiss temperature $\theta_{CW} = -21$ K, and the spin entropy S_{mag} at T_N amounts to approximately 40% of $R[0.7 \times \ln4 + 0.16 \times \ln5]$. The presence of the magnetic entropy in an order of θ_{CW} and the relatively moderate entropy release at T_N are common to frustrated spin systems.[32,33] The total S_{mag} approaches the expected theoretical value of 10.21 J/(mol·K) for the mixed Mn^{4+} ($S = 3/2$) and Mn^{3+} ($S = 2$) spins at $T = 150$ K. The persistence of short-range correlations to the CW temperature suggests that low-dimensional, frustrated spin dynamics is not fully quenched despite its relatively large spin number. We recall that the $S = 3/2$ triangular Heisenberg antiferromagnetic NaCrO$_2$[34] is comparable to our studied compound. Thus, our SMTO compound bears dynamical features inherent to a classical frustrated spin system.

Furthermore, we measured $C_p(T)$ at different magnetic fields $\mu_0H = 0-9$ T for $H\|ab$. As shown in Figure 6, with increasing magnetic field, the broad maximum shifts from $T_N = 6.54$ K at 0 T to 6.19 K at 9 T. The essentially same trend is
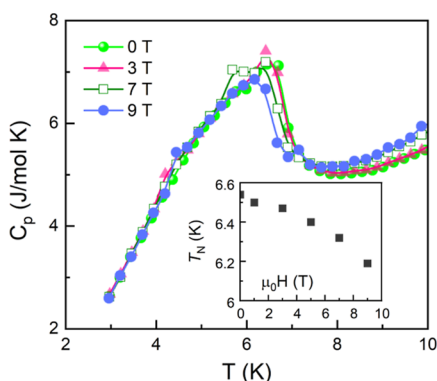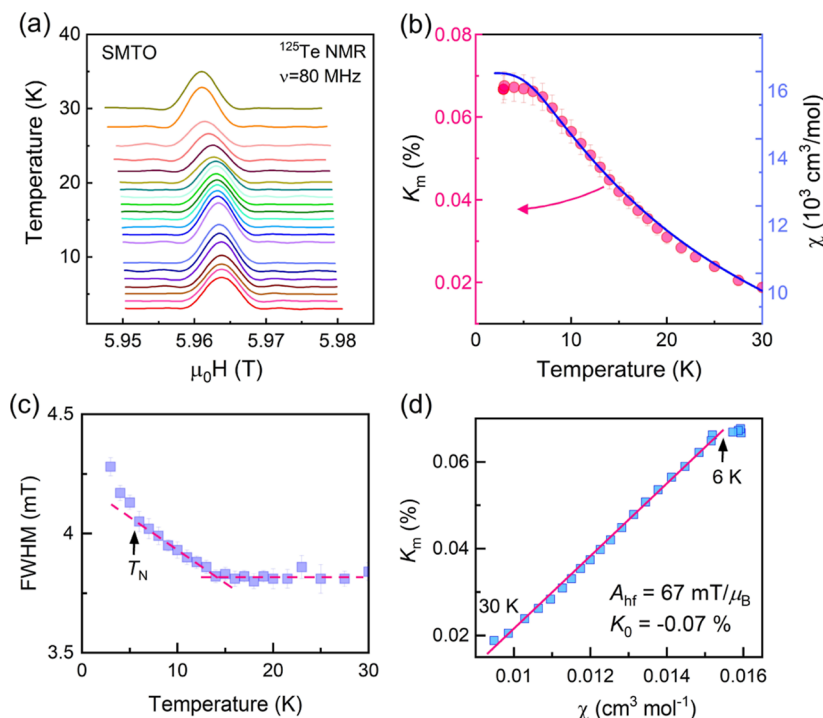
Figure 6. C_p vs temperature of SMTO single crystal measured at various magnetic fields $\mu_0 H = 0, 3, 7$, and 9 T for $H \| ab$. The inset plots the Néel temperature vs an external magnetic field.

observed from $\chi(T)$ (as compared to the inset of Figure 6 with Figure 3e,f).

3.6. ^{125}Te NMR. In order to clarify spin dynamics and dynamical magnetic behaviors, we carried out NMR measurements. The ^{125}Te ($I = 1/2$) NMR spectra of SMTO measured at a frequency of $\nu = 80$ MHz are shown in Figure 7a. The crystal is aligned in a field direction along the c-axis, the field-swept spectra are composed of a single peak, which is well described by a single Gaussian function in the temperature range of $T = 4{-}30$ K. Additionally, we note that two Gaussian functions give a better description of the $T = 3$ K spectrum, indicative of the peak splitting of 3×10^{-3} T (not shown here). Since the field inhomogeneity of our NMR setup is an order of $\sim 2 \times 10^{-4}$ T/mm, the field inhomogeneity effect is less likely to affect the NMR signal.

With decreasing temperature, the peak shifts toward higher fields, which is proportional to $\chi(T)$ (Figure 7b). As shown in Figure 7c, the line width starts to broaden linearly on cooling below 14 K and shows deviation from a linear increase at $T_N = 6.54$ K. The line broadening points toward the development of critical spin fluctuations. We stress that the onset temperature of the line broadening corresponds to the weak maximum temperature of C_{mag} (see the inset of Figure 5a). Nonetheless, the absence of apparent line splitting may be due to the compensation of the staggered local magnetic fields generated by a Néel-type magnetic order. However, we cannot exclude the possibility that field inhomogeneity and antisite defects partly obscure a line splitting.

The relative shift of the NMR line is caused by the local magnetic fields and is defined by $K = (f_{peak} - f_0)/f_0 \times 100$ (%), where $f_0 = \gamma_N H_0$ and f_{peak} is the frequency of the peak. The NMR shift comprises two contributions $K(T) = K_0 + K_m(T)$, where K_0 is the temperature-dependent term (called a chemical or orbital shift), which stems from the coupling with the Te electrons, and $K_m(T)$ is the temperature-dependent magnetic shift through the hyperfine coupling with the Mn^{4+}/Mn^{3+} spins. Figure 7b presents the temperature dependence of the magnetic shift $K_m(T)$, which reflects the intrinsic magnetic susceptibility $\chi(T)$. As the temperature is lowered to 30 K, $K_m(T)$ increases to higher values and then flattens out. This resemblance is apparently seen in the magnetic susceptibility $\chi(\mu_0 H = 5.96$ T) plotted together with $K_m(T)$ (see the blue line in Figure 7b). By correlating $K_m(T)$ with $\chi(T)$ with temperature as an implicit parameter, one can extract information about the transferred hyperfine interaction A_{hf} between the ^{125}Te nuclear spins and the Mn^{4+}/Mn^{3+} electron

Figure 7. (a) Field-swept ^{125}Te NMR spectra of a single crystal of SMTO were recorded by integrating spin-echo intensity as a function of temperature. (b) Temperature dependence of the magnetic shift $K_m(T)$ of the ^{125}Te nuclear spins plotted together with the static magnetic susceptibility. (c) Line width of the ^{125}Te NMR spectra as a function of temperature. The dashed lines are a linear guide to the eye. (d) Plot of a magnetic shift vs dc susceptibility. The solid line is the fit using eq 2.

spins. In this so-called Clogston-Jaccarino $K_m-\chi$ plot, $K_m(T)$ is fitted to the equation

$$K_m(T) = K_0 + \left(\frac{A_{hf}}{N_A \mu_B}\right)\chi(T) \tag{2}$$

where the zero intercept gives the orbital shift K_0. The shift data fit in the temperature range $T = 6-30$ K yields the hyperfine coupling constant $A_{hf} = 0.067$ T/μ_B (see the red line in Figure 7d).

To probe spin dynamics, we investigated the ^{125}Te nuclear spin−lattice relaxation rate $1/T_1$ in the temperature range of $T = 3-30$ K, which crosses the magnetic transition at $T_N = 6.6$ K. Noteworthy is that the chosen temperature window is sufficiently wide to trace the development of magnetic correlations from the paramagnetic to the magnetically ordered region.

Figure 8 exhibits the temperature dependence of $1/T_1$. As shown in the inset of Figure 8, on cooling from 30 K, $1/T_1$
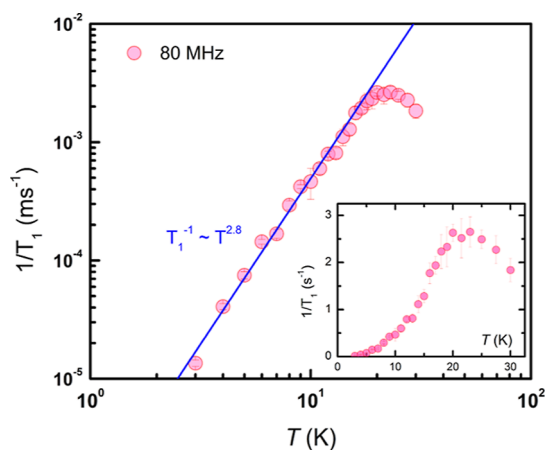
Figure 8. ^{125}Te spin−lattice relaxation rate $1/T_1$ vs temperature on a log−log plot. The inset shows $1/T_1$ on a normal scale.

increases and then forms a broad maximum at about 21 K and finally decreases rapidly. $1/T_1$ does not show a λ-like peak at T_N. The lacking λ-like divergence may be related to the near cancellation of the staggered local magnetic fields and the antisite defects. Instead, $1/T_1$ exhibits a broad maximum in the temperature scale of the CW temperature. This temperature scale is somewhat higher than the weak maximum temperature of C_{mag}. In the short-range ordered state ($T = 6-18$ K), $1/T_1$ displays the power-law dependence $1/T_1 \sim T^{2.8}$, as evident from the log−log plot in Figure 8. This is reminiscent of a T^3 behavior in antiferromagnets.[35] In a magnetically ordered state, $1/T_1$ is dictated by the scattering of magnons off nuclear spins. If a two-magnon Raman process is dominant, the relaxation follows the T^3 dependence. The observed T^3-like dependence of $1/T_1$ well above T_N may indicate that two-dimensional magnons are present in the studied compound. Future neutron scattering experiments are envisioned to determine a magnetic ordering pattern below T_N and to identify two-dimensional magnon-like excitations for temperatures above T_N.

4. CONCLUSIONS

In summary, single crystals of an emergent triangular lattice SMTO were grown successfully using a self-flux growth method. The previously reported $P\bar{6}2m$ structure of

SrMnTeO$_6$ with cations in prismatic coordination has been revised using NPD and SCXRD. It is shown unambiguously that SMTO belongs to the chiral space group $P312$ with all cations in octahedral coordination. The dc magnetic susceptibility and heat capacity measurement reveal the occurrence of a weak antiferromagnetic order at $T_N = 6.6$ K. Isothermal magnetization ($M-H$ curve) increases linearly with increasing magnetic field without any hysteresis, which is characteristic of antiferromagnets. This supports the non-negligible magnetic frustration parameter $f \sim 3.05$ extracted from the magnetic susceptibility analysis. We recall that the frustration parameter of SMTO is larger than $f \sim 2.16$ of PbMnTeO$_6$, evincing that the (B, B′) cation ordering tends to increase the magnetic frustration despite a small fraction of antisite defects. The magnetic entropy and the ^{125}Te nuclear spin−lattice relaxation rate show the persistence of short-range magnetic correlations to $\sim 3T_N$ and the characteristic temperature scale of 14−21 K associated with low-dimensional short-range ordering. Most remarkably, magnon-like excitations persist to the temperature scale of $3T_N$.

■ ASSOCIATED CONTENT

■ AUTHOR INFORMATION

Corresponding Author

Raman Sankar − *Institute of Physics, Academia Sinica, Taipei 11529, Taiwan;* ⊙ orcid.org/0000-0003-4702-2517; Email: sankarraman@gate.sinica.edu.tw, sankarndf@gmail.com

Authors

Kalimuthu Moovendaran − *Institute of Physics, Academia Sinica, Taipei 11529, Taiwan*

Raju Kalaivanan − *Institute of Physics, Academia Sinica, Taipei 11529, Taiwan*

I. Panneer Muthuselvam − *Department of Physics (MMV), Banaras Hindu University, Varanasi, Uttar Pradesh 221005, India;* ⊙ orcid.org/0000-0002-7763-5915

K. Ramesh Babu − *Department of Physics, National Taiwan University, Taipei 10617, Taiwan; Physics Division, National Center for Theoretical Sciences, Hsinchu 30013, Taiwan*

Suheon Lee − *Department of Physics, Chung-Ang University, Seoul 06974, Republic of Korea*

C. H. Lee − *Department of Physics, Chung-Ang University, Seoul 06974, Republic of Korea*

Khasim Saheb Bayikadi − *Institute of Physics, Academia Sinica, Taipei 11529, Taiwan*

Namasivayam Dhenadhayalan − *Department of Chemistry, National Taiwan University, Taipei 10617, Taiwan;* ⊙ orcid.org/0000-0003-4494-5746

Wei-Tin Chen − *Center for Condensed Matter Sciences and Center of Atomic Initiative for New Materials, National*

Taiwan University, Taipei 10617, Taiwan; Taiwan Consortium of Emergent Crystalline Materials, Ministry of Science and Technology, Taipei 10622, Taiwan

Chin-Wei Wang − National Synchrotron Radiation Research Center, Hsinchu 30076, Taiwan; orcid.org/0000-0001-9012-2420

Yen-Chung Lai − National Synchrotron Radiation Research Center, Hsinchu 30076, Taiwan

Yoshiyuki Iizuka − Institute of Earth Sciences, Academia Sinica, Taipei 11529, Taiwan

Kwang-Yong Choi − Department of Physics, Sungkyunkwan University, Suwon 16419, Republic of Korea; orcid.org/0000-0001-8213-5395

Vladimir B. Nalbandyan − Chemistry Faculty, Southern Federal University, Rostov-on-Don 344090, Russia; orcid.org/0000-0002-8624-0165

Complete contact information is available at:
https://pubs.acs.org/10.1021/acs.inorgchem.2c01585

Notes
The authors declare no competing financial interest.

■ REFERENCES

(1) Hill, N. A. Why Are There so Few Magnetic Ferroelectrics? *J. Phys. Chem. B* **2000**, *104*, 6694−6709.

(2) Ederer, C.; Spaldin, N. A. Recent Progress in First-Principles Studies of Magnetoelectric Multiferroics. *Curr. Opin. Solid State Mater. Sci.* **2005**, *9*, 128−139.

(3) Khomskii, D. Classifying Multiferroics: Mechanisms and Effects. *Phys.* **2009**, *2*, 20.

(4) Cheong, S. W.; Mostovoy, M. Multiferroics: A Magnetic Twist for Ferroelectricity. *Nat. Mater.* **2007**, *6*, 13−20.

(5) Wang, P. S.; Ren, W.; Bellaiche, L.; Xiang, H. J. Predicting a Ferrimagnetic Phase of Zn_2FeOsO_6 with Strong. *Magnetoelectric Coupling* **2015**, *114*, 1−6.

(6) Young, J.; Stroppa, A.; Picozzi, S.; Rondinelli, J. M. Tuning the Ferroelectric Polarization in $AA'MnWO_6$ double Perovskites through A Cation Substitution. *Dalton Trans.* **2015**, *44*, 10644−10653.

(7) Kinoshita, M.; Seki, S.; Sato, T. J.; Nambu, Y.; Hong, T.; Matsuda, M.; Cao, H. B.; Ishiwata, S.; Tokura, Y. Magnetic reversal of electric polarization with fixed chirality of magnetic structure in a chiral-lattice helimagnet $MnSb_2O_6$. *Phys. Rev. Lett.* **2016**, *117*, 047201.

(8) Hill, R. J. Structure of $PbSb_2O_6$ and Its Relationship to the Crystal Chemistry of PbO_2 in Antimonial Lead-Acid Batteries. *J. Solid State Chem.* **1987**, *71*, 12−18.

(9) Rao, G. N.; Sankar, R.; Muthuselvam, I. P.; Chou, F. C. Magnetic and thermal property studies of $RCrTeO_6$ (R = trivalent lanthanides) with layered honeycomb sublattices. *J. Magn. Magn. Mater.* **2014**, *370*, 13−17.

(10) Liu, J.; Ouyang, Z.; Liu, X.; Cao, J.; Wang, J.; Xia, Z.; Rao, G. Decoupling of Gd-Cr magnetism and giant magnetocaloric effect in layered honeycomb tellurate $GdCrTeO_6$. *J. Appl. Phys.* **2020**, *127*, 173902.

(11) Kim, S. W.; Deng, Z.; Fischer, Z.; Lapidus, S. H.; Stephens, P. W.; Li, M. R.; Greenblatt, M. Structure and Magnetic Behavior of Layered Honeycomb Tellurates, $BiM(III)TeO_6$ (M = Cr, Mn, Fe). *Inorg. Chem.* **2016**, *55*, 10229−10237.

(12) Matsubara, N.; Petit, S.; Martin, C.; Fauth, F.; Suard, E.; Rols, S.; Damay, F. $BiMnTeO_6$: A multiaxis Ising antiferromagnet. *Phys. Rev. B* **2019**, *100*, 220406.

(13) Phatak, R.; Krishnan, K.; Kulkarni, N.; Achary, S.; Banerjee, A.; Sali, S. Crystal structure, magnetic and thermal properties of $LaFeTeO_6$. *Mater. Res. Bull.* **2010**, *45*, 1978−1983.

(14) Zvereva, E.; Vasilchikova, T.; Evstigneeva, M.; Tyureva, A.; Nalbandyan, V.; Gonçalves, J.; Barone, P.; Stroppa, A.; Vasiliev, A. Chirality and Magnetocaloricity in $GdFeTeO_6$ as Compared to $GdGaTeO_6$. *Materials* **2021**, *14*, 5954.

(15) Woodward, P. M.; Sleight, A. W.; Du, L. S.; Grey, C. P. Structural Studies and Order-Disorder Phenomenon in a Series of New Quaternary Tellurates of the Type $A^{2+}M^{4+}Te^{6+}O_6$ and $A^{1+}_2M^{4+}Te^{6+}O_6$. *J. Solid State Chem.* **1999**, *147*, 99−116.

(16) Kim, S. W.; Deng, Z.; Yu, S.; Padmanabhan, H.; Zhang, W.; Gopalan, V.; Jin, C.; Greenblatt, M. $A(II)GeTeO_6$ (A = Mn, Cd, Pb): Non-Centrosymmetric Layered Tellurates with $PbSb_2O_6$ Related Structure. *Inorg. Chem.* **2017**, *56*, 9019−9024.

(17) Kuchugura, M. D.; Kurbakov, A. I.; Zvereva, E. A.; Vasilchikova, T. M.; Raganyan, G. V.; Vasiliev, A. N.; Barchuk, V. A.; Nalbandyan, V. B. $PbMnTeO_6$: A Chiral Quasi 2D Magnet with All Cations in Octahedral Coordination and the Space Group Problem of Trigonal Layered $A^{2+}M^{4+}TeO_6$. *Dalton Trans.* **2019**, *48*, 17070−17077.

(18) Ding, F.; Nisbet, M. L.; Yu, H.; Zhang, W.; Chai, L.; Halasyamani, P. S.; Poeppelmeier, K. R. Syntheses, Structures, and Properties of Non-Centrosymmetric Quaternary Tellurates $BiMTeO_6$ (M = Al, Ga). *Inorg. Chem.* **2018**, *57*, 7950−7956.

(19) Wulff, L.; Müller-Buschbaum, H. Isolierte trigonale SrO_6-Prismen verknüpfen Kagome-Netze im Strontium-Manganat (IV)-Tellurat (VI): $SrMnTeO_6$. *Z. Naturforsch., B: J. Chem. Sci.* **1998**, *53*, 283−286.

(20) Kim, S. W.; Deng, Z.; Li, M. R.; Sen Gupta, A.; Akamatsu, H.; Gopalan, V.; Greenblatt, M. $PbMn(IV)TeO_6$: A New Noncentrosymmetric Layered Honeycomb Magnetic Oxide. *Inorg. Chem.* **2016**, *55*, 1333−1338.

(21) Waroquiers, D.; Gonze, X.; Rignanese, G.-M.; Welker-Nieuwoudt, C.; Rosowski, F.; Göbel, M.; Schenk, S.; Degelmann, P.; André, R.; Glaum, R.; Hautier, G. Statistical Analysis of Coordination Environments in Oxides. *Chem. Mater.* **2017**, *29*, 8346−8360.

(22) Nakatsuji, S.; Nambu, Y.; Tonomura, H.; Sakai, O.; Jonas, S.; Broholm, C.; Tsunetsugu, H.; Qiu, Y.; Maeno, Y. Physics: Spin Disorder on a Triangular Lattice. *Science* **2005**, *309*, 1697−1700.

(23) Ramirez, A. P.; Hessen, B.; Winklemann, M. Entropy Balance and Evidence for Local Spin Singlets in a Kagomé-like Magnet. *Phys. Rev. Lett.* **2000**, *84*, 2957−2960.

(24) Inami, T.; Nishiyama, M.; Maegawa, S. Magnetic Structure of the Kagomé Lattice Antiferromagnet Potassium Jarosite. *Phys. Rev. B: Condens. Matter Mater. Phys.* **2000**, *61*, 12181−12186.

(25) Katsura, S.; Ide, T.; Morita, T. The Ground States of the Classical Heisenberg and Planar Models on the Triangular and Plane Hexagonal Lattices. *J. Stat. Phys.* **1986**, *42*, 381−404.

(26) Liss, K. D.; Hunter, B.; Hagen, M.; Noakes, T.; Kennedy, S. Echidna-the New High-Resolution Powder Diffractometer Being Built at OPAL. *Phys. B Condens. Matter* **2006**, *385−386*, 1010−1012.

(27) Rodriguez-Carvajal, J. "Fullprof: A Program for Rietveld Refinement and Pattern Matching Analysis". *Abstract of the Satellite Meeting on Powder Diffraction of the XV Congress of the IUCr*; Scientific Research Publishing: Toulouse, France, 1990; p 127.

(28) Sheldrick, G. M. Crystal structure refinement with SHELXL. *Acta Crystallogr.* **2015**, *71*, 3−8.

(29) Shannon, R. D. Revised Effective Ionic Radii and Systematic Studies of Interatomic Distances in Halides and Chalcogenides. *Acta*

Crystallogr., Sect. A: Cryst. Phys., Diffr., Theor. Gen. Crystallogr. **1976**, *32*, 751.

(30) Ramirez, A. P. Strongly Geometrically Frustrated Magnets. *Annu. Rev. Mater. Sci.* **1994**, *24*, 453−480.

(31) Muthuselvam, I. P.; Sankar, R.; Ushakov, A. V.; Rao, G. N.; Streltsov, S. V.; Chou, F. C. Two-Step Antiferromagnetic Transition and Moderate Triangular Frustration in $Li_2Co(WO_4)_2$. *Phys. Rev. B: Condens. Matter Mater. Phys.* **2014**, *90*, 1−7.

(32) Koteswararao, B.; Kumar, R.; Khuntia, P.; Bhowal, S.; Panda, S. K.; Rahman, M. R.; Mahajan, A. V.; Dasgupta, I.; Baenitz, M.; Kim, K. H.; Chou, F. C. Magnetic Properties and Heat Capacity of the Three-Dimensional Frustrated S= 1/2 Antiferromagnet $PbCuTe_2O_6$. *Phys. Rev. B: Condens. Matter Mater. Phys.* **2014**, *90*, 1−7.

(33) Zhou, H. D.; Choi, E. S.; Li, G.; Balicas, L.; Wiebe, C. R.; Qiu, Y.; Copley, J. R. D.; Gardner, J. S. Spin Liquid State in the S=1/2 Triangular Lattice $Ba_3CuSb_2O_9$. *Phys. Rev. Lett.* **2011**, *106*, 147204−147207.

(34) Olariu, A.; Mendels, P.; Bert, F.; Ueland, B. G.; Schiffer, P.; Berger, R. F.; Cava, R. J. Unconventional Dynamics in Triangular Heisenberg Antiferromagnet $NaCrO_2$. *Phys. Rev. Lett.* **2006**, *97*, 2−5.

(35) Beeman, D.; Pincus, P. Nuclear Spin-Lattice Relaxation in Magnetic Insulators. *Phys. Rev.* **1968**, *166*, 359−375.